Technical Paper

Applicability of ultra-high-resolution 3D seismic data for geohazard identification at mid-slope depths in the Gulf of Mexico: Initial results

Brian N Brookshire, Jr*[1], Frank P Landers[2] and Jaime A Stein[2]

[1]NCS SubSea, 3928 Bluebonnet Drive, Stafford, TX 77477

[2]Geotrace Technologies, 12141 Wickchester Lane, Suite 200, Houston, TX 77079

Abstract

Preliminary results from data collected along mid-slope depths in the northern Gulf of Mexico are very promising in regard to the applicability of short offset, ultra-high-resolution, three-dimensional (UHR3D) seismic methods in the detection and delineation of geohazards. Penetration of greater than 2s two-way travel time (TWT) below seabed was achieved with a P-Cable™ system comprising 18 streamers that were 100m in length and a 210in³ Generator-Injector (GI) air gun fired in harmonic mode. Dips in excess of 17° were imaged at greater than 1s TWT below the sea floor. Between the sea floor and 1s TWT below the sea floor, the dominant frequency recovered is between about 78Hz and 100Hz. Apparent subsurface horizontal resolution is in the order of 16m, and subsurface vertical resolution is as high as 1.6m. Seafloor resolution is consistent with the natural bin size of 3.125 × 6.25m.

Keywords: UHR3D, high-resolution seismic, three-dimensional seismic, Gulf of Mexico, P-Cable, geohazard

1. Introduction

1.1. General significance of ultra-high-resolution, three-dimensional seismic methods

Ultra-high-resolution, three-dimensional (UHR3D) seismic acquisition refers to seismic data collected in three dimensions with a high frequency acoustic source (dominant frequency ~80Hz to 1kHZ), a very high sample rate ($\geq$2,000Hz) and a very small bin size (<12.5m cross-line). In practice, UHR3D seismic acquisition is also characterised by very short offsets, low angles of incidence, low fold and a narrow central measurement point swath relative to traditional 3D seismic acquisition. These practical limitations are not mentioned as a negative, but as an affirmation that UHR3D seismic acquisition is very different from exploration 3D seismic acquisition, and even high-resolution 3D seismic acquisition – which is often designated simply by the frequency content of the resultant data (Sheriff, 2002).

Successful UHR3D seismic acquisition requires a low-noise receiver array, a high-fidelity recording system, a high cycle-rate seismic source system, excellent positioning and good sampling/constraint of near-surface statics. In addition, because of the smaller scale of the receiver array, a well thought out acquisition geometry must be employed along with a keen monitoring of environmental conditions and their effect on the in-water spread. While it might be argued that these are requisites of any successful seismic survey, traditional challenges experienced in processing marine seismic data are significantly exaggerated. This is because of the extremely high sampling rate (which is necessary to preserve the wavelet when recording high-frequency data), as well as the very small bin size. Traditional tolerances in accuracy and precision are no longer applicable, and small errors are no longer trivial.

In the last few years, concurrent with the development of several UHR3D seismic acquisition systems/methodologies, the oil and gas industry has spoken out regarding the need for something beyond traditional 3D and high-resolution two-dimensional (2D) methods for site survey and geohazard identification (Games, 2012). The advantages of UHR3D seismic acquisition are not necessarily a difficult sell, but particularly in the Gulf of Mexico, with its complex, salt-related geology, the financial risk versus reward of UHR3D seismic techniques has been widely questioned. What penetration can be

---

* Contact author. Email address: brian.brookshire@ncs-subsea.com

expected? What bandwidth will be recovered? What sort of resolution will be achieved? Can steep dips be resolved in intermediate to deep water effectively with such short offsets? The intention of this preliminary study is to answer these basic, but important, questions by providing a concise overview of the methodology and initial results from a very recent (June to August 2014) project. This project utilised UHR3D seismic techniques at mid-shelf depths in the Gulf of Mexico (~1,000m) over complex, salt-related geology.

1.2. Acquisition system

The P-Cable™ seismic system was chosen for the present study. This system employs multiple short streamers towed from a cross-cable diverted between two vanes (Fig 1). Because the heads of the relatively short streamers are fixed along the cross-cable, the cross-line streamer spacing can be very low by design. This system has been utilised extensively in the Barents Sea, where researchers have effectively imaged gas chimneys and fluid flow structures (Petersen et al., 2010; Plaza-Faverola et al., 2011). Here, the resolution has been sufficient to image truncated, paleo fluid flow structures and active structures with a modern seafloor expression. In the Gulf of Cadiz, the P-Cable™ technology has been used to image complex tectonic faulting and other clues as to the nature of active deformation in the region (Crutchley et al., 2011). Offshore Montserrat, the P-Cable™ technology was used to assess emplacement dynamics of past volcanic landslides (Crutchley et al., 2013). Of particular note, researchers were

successful in imaging fold-related fault successions and steeply dipping coherent reflectors.

In the present study, the P-Cable™ receiver array was positioned using a proprietary solution designed specifically for the application. The solution employs compasses and depth sensors along the cross-cable at the head of each streamer, redundant global positioning system (GPS) receivers at the ends of the cross-cable (tripoints and vanes), and compasses at the tail of each streamer. The algorithm collects observations from the sensors and, via an iterative least-squares process, models the shape of the cross-cable to derive a position for the heads of the streamers. Utilising the tail compass data from the relatively short streamers, an absolute position for each receiver group is calculated. This solution is applicable to the P-Cable™ because of the relatively small size of the array and the relative stability of the array under tow.

The GeoEel Solid™ streamers are held under tension by low-profile drogues affixed to the tails of the streamers and suffer little to no meandering movement. Likewise, the streamers are neutrally buoyant, and the depth at the head of the streamer reasonably translates to the depth at the tail of the streamer. In an operational sense, this solution is particularly attractive because there is no need for externally affixed birds and/or acoustics that would inevitably lead to tangles on deployment and recovery. In conjunction with real-time GPS-based source positioning, this solution provides a real-time delineation of the receiver array and a real-time binning display. Therefore, the surveyor
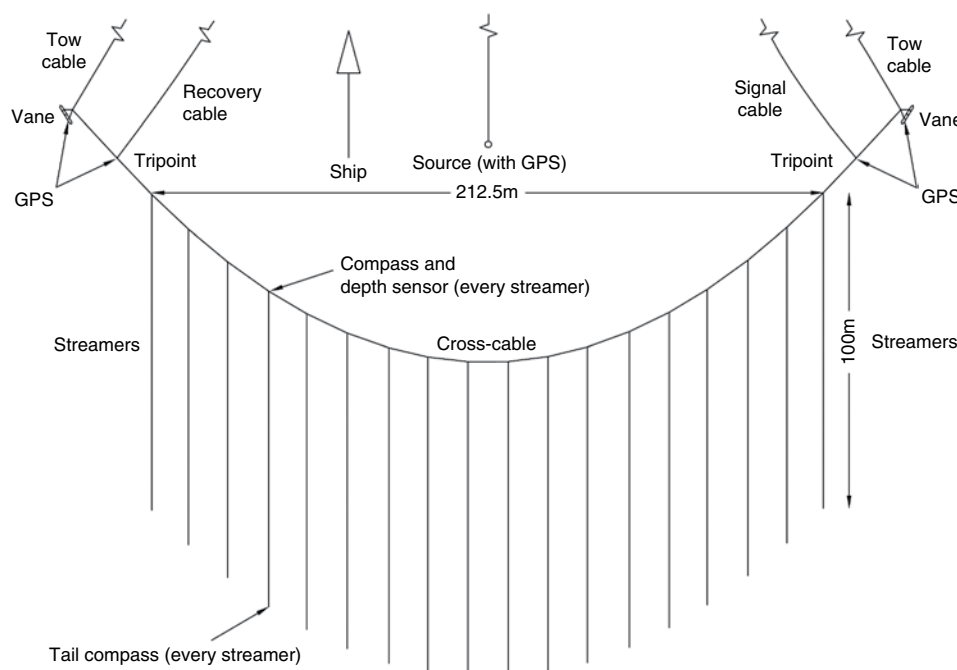

Fig 1: Scaled diagram of the P-Cable™ system under deployment

is equipped with all of the information necessary to monitor the geometry of the spread and steer 3D coverage. To the authors' knowledge, the present paper represents the first documentation of such detailed positioning of the receiver array. Previous studies have positioned the receiver array during acquisition based on an assumed cross-cable shape, with post-acquisition positioning refinements based on first breaks (direct arrivals; e.g. Petersen et al., 2010).

1.3. Survey setting

These data were collected around mid-slope (~700–1,000m) on the Gulf of Mexico continental slope in the four corners area proximal to Atwater Valley Block 047. The area is geologically and oceanographically complex, characterised by intraslope basins interrupted by diapiric and tabular salt features (Bryant et al., 1990; Diegel et al., 1995; Prather et al., 1998). This area on the Gulf of Mexico slope has numerous occurrences of hydrocarbon seepage, mud mounds and gas hydrates (Brooks et al., 1986; MacDonald et al., 1994; Roberts, 2001; Sager et al., 2003). In addition, this area is oceanographically influenced by the Gulf of Mexico Loop Current and associated mesoscale eddies (Sturges and Leben, 2000). A thorough discussion of this complexity is beyond the scope of the present paper.

2. Methods

2.1. Receiver array, geometry and recording parameters

The fundamental component of the receiver array is the GeoEel Solid™ streamer. The streamers were purpose built with a receiver group spacing of 6.25m and 12 hydrophones per group, providing over 4 octaves of bandwidth and a low cut of approximately 5Hz. Each deployed streamer consists of two sections with eight groups per section, yielding 100m streamers with a total of 16 channels. Eighteen streamers (288 groups) were deployed along the cross-cable with a nominal cross-line spacing of 12.5m. The nominal towing depth of the streamers was approximately 2m as relegated by the depth of the crucifix of the vanes.

The cross-cable assumes a catenary-like shape under tow. Therefore, the actual spacing of the streamer takeouts along the cross-cable was scaled so that the nominal cross-line spacing equalled 12.5m when the cross-cable was at the desired shape, quantified as the shortening factor. The shortening factor is defined as the cross-line distance between the streamer 1 and streamer 18 takeout, divided by the total distance along the cross-cable between the streamer 1 and streamer 18 takeout. The shortening

factor is controlled by the separation, or amount of pull, generated by the paravanes.

A full-scale, static test was performed in order to determine what shortening factor is most favoured by the positioning algorithm, and this was the reference for both the design and acquisition geometry specifications of the system. The 6.25m inline by 12.5m cross-line group spacing yields a natural common-midpoint (CMP) bin size of 3.125m inline and 6.25m cross-line. The total surface coverage of the receiver array at the nominal shortening factor is 212.5m, and the CMP coverage is 106.25m. Line spacing was 100m, providing two bins of overlap between adjacent passes. The line heading was along slope at a bearing of 57°/237°.

The recording system was configured with a sample rate of 0.25ms and a record length of 4.5s. Through the recording software, the digitisers were set with a pre-amp gain of 18dB. The target vessel speed was 4.0 knots over-ground, which yields approximately 6s between shots when shooting on distance at a 12.5m shot-point spacing. A 12.5m shooting interval provides nominal 4 fold coverage at the natural bin size (3.125×6.25m). The data were recorded according to the Society of Exploration Geophysicist (SEG) convention of minimum phase, normal polarity.

2.2. Energy source

A single Sercel 210in^3 Generator-Injector (GI) gun was chosen as the energy source for the survey. The gun was configured to fire in harmonic mode with the generator injector delay set based on the nominal towing depth of 3m. The generator and injector volumes were set to be equal at 105in^3 per volume. The near-field signature of the gun was actively recorded as a quality control (QC) measure to ensure performance and repeatability of the source. A far-field signature was also collected so that the data could be de-signatured in processing.

The position of the source relative to the receiver array was set such that the energy source was as equidistant as possible from all 288 receiver groups. This resulted in a range of angles of incidence between approximately 1.5° and 3.5° based on a horizontal reflector 1,500m below the acquisition system. The range of horizontal azimuths was approximately 160°.

2.3. Environmental constraints

Local sea surface elevation was constantly measured relative to the mean sea surface using a Veripos differential GPS precise point positioning system and the Verify QC Tides software. These data were measured at 1s intervals and averaged over 1min periods. Water column sound velocity data were collected with a Sippcan system and extended

depth XSV-02 probes. These probes were launched at semi-regular intervals based on a pre-gridding measurement scheme amounting to nine probes per 320km² area.

2.4. Seismic data processing

The seismic data, collected at a 4,000Hz sampling rate, are downsampled and processed at 2,000Hz. The idea behind the extremely high-acquisition sampling rate is that the field data may be reprocessed in the future when more advanced algorithms can fully take advantage of the density of data recorded and the very small amplitude high frequencies recorded. The data presented here are from a fast-track, initial volume, having only gone through navigation merge, basic wavelet processing, noise elimination, static corrections, post-stack time migration and some basic post migration processing. These data have not undergone deghosting, surface-related multiple elimination (SRME), or any other advanced processing techniques. Therefore, the examples presented here are a conservative representation of data quality and the level of processing.

2.5. Navigation data processing

Raw UK Offshore Operators Association (UKOOA) P2/94 format navigation data were edited to remove spikes and, in some cases, smoothed. Once the editing process was complete and the parameters for the network adjustment were input, the data were processed with the same least-squares-based algorithm used in positioning the P-Cable™ array and sourced in real time. Early on, the processing of the data involved some trial and error in order to determine the most appropriate values for an *a priori* standard deviation of the GPS and compass measurements, as well as for the stretch of the cross-cable. Once settled on, these values were employed consistently depending on which combination of endpoint GPS units was used. Following the network adjustment, the processed navigation data were output in UKOOA P1/90 format for merging with the seismic data.

3. Results

3.1. Penetration, dip imaging and bandwidth

Fig 2 provides a representative illustration of the level of penetration achieved. There are clear, coherent amplitudes present at greater than 3s two-way travel time (TWT). This equates to over 2s TWT penetration below the sea floor. Very importantly, Fig 2 also illustrates that there is very good imaging below the seafloor multiple. The seafloor multiple crosscuts a unit of strong, likely gas charged, reflectors at trace 61600 and 2.000s TWT. Also of note in this figure are the relatively steeply dipping reflections centred at about trace 62750 and 2.250s TWT. Though not inferable here, these reflectors are uplifted as a result of salt diapirism further
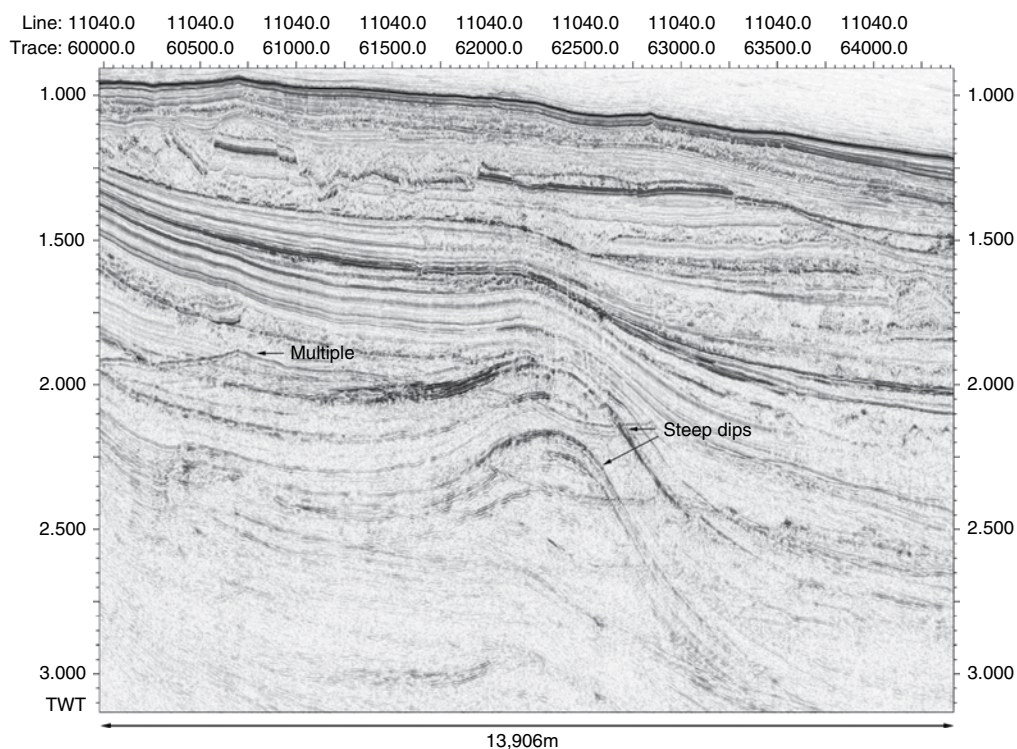

Fig 2: Seismic profile illustrating penetration, the presence of data below the sea floor multiple and steep dips

developed in the cross-line direction. Based on the simple equation provided by Marfurt (2006), the relationship between apparent time dip (p) (in s/m) and the apparent angle dip (θ_x) (in degrees) in the inline direction can be expressed as:

$$p = \frac{2Tan\theta_x}{v} \qquad (1)$$

When applying this equation to determine the approximate maximum apparent angle dip of this feature over an inline distance of 218.8m, using a velocity (v) of 1,650m/s, the result is at an inline apparent angle dip of 17.2°. The velocity of 1,650m/s represents the root-mean-square velocity at the approximate TWT and location of the measured dips based on a velocity model generated from numerous check-shot surveys in the area.

Single (stacked) trace frequency spectra taken from the vicinity of the data discussed earlier reveal very high dominant frequencies and a broad bandwidth recovery. Fig 3 illustrates the frequency spectrum from the sea floor to 0.500s TWT below the sea floor (upper window), overlain with the frequency spectrum from 0.500s to 1.000s TWT below the sea floor (lower window). The dominant frequency in the upper window is 99.6Hz, with a low end 50% relative amplitude threshold of 56.6Hz and a high end 50% relative amplitude threshold of 166.0Hz. The dominant frequency in the lower window is 78.1Hz, with a low end 50% relative amplitude threshold of 64.5Hz and a high end 50% relative amplitude threshold of 138.7Hz. Further depths were not considered here because these data have not been through SRME and similar advanced processing techniques to remove multiple reflections.

3.2. Resolution

The horizontal resolution of the data is a function of the natural bin size (3.125 × 6.25m), the quality
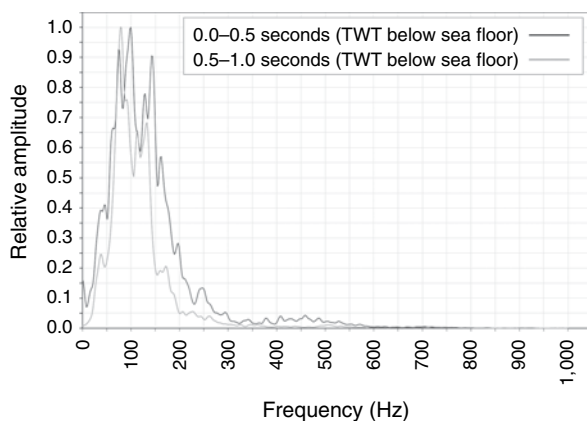

Fig 3: Frequency spectrum measured over 0.500s intervals for the first 1s TWT below the sea floor

of the navigation data and the frequency content of the recorded signal (which impacts spatial aliasing). At a natural bin size of 3.125 × 6.25m, a dip of 17.2° and an assumed velocity of 1,600m/s, the maximum unaliased frequency in the inline direction is 432.9Hz and the maximum unaliased frequency in the cross-line direction is 216.4Hz (Vermeer, 2012). In the present study, given the dominant frequency content of the recorded signal (as discussed earlier), and the aliasing frequencies for the bin dimensions, it is clear that the frequency content is not limiting the spatial resolution.

The vertical resolution hinges on numerous static corrections, but fundamentally is controlled by the sampling interval and the recovered frequencies. At a 2,000Hz sample rate, the Nyquist frequency is 1,000Hz (Sheriff, 2002), which is very high indeed. So, in the case of the data in the present study, the major limiting factor in vertical resolution is recovered frequency. If the dominant frequencies for the upper 1s is taken (as discussed earlier) and these numbers are related to vertical resolution using the relationship of the Rayleigh resolution limit ($\lambda/4$; Sheriff, 2002), the theoretical vertical resolution limit for the upper 0.500s is 4.0m, and 5.1m for 0.500–1.000s TWT below the sea floor. These figures assume a constant velocity of 1,600m/s, and that the limit of resolution is completely relegated by the dominant frequency. In fact, even with these preliminarily, post-stack migrated data, the apparent vertical resolution is much greater.

Fig 4 illustrates numerous aspects of the shallow subsurface resolution achieved with the data. This figure is a perspective chair-cut representation illustrating data in both time slice and profile views with blow-ups of very fine-scale features of particular relevance. Fine-scale faulting and folding is visible across the centre of the time slice, and there are multiple expulsion features present. Of particular note is the circular gas anomaly, which is interpreted to be free gas below a gas hydrate mound (McDonald et al., 1994; Holbrook, 2001). The blow-ups illustrate the very fine spatial and vertical resolution of the data. The right blow-up (Fig 4c) highlights faults and displaced blocks as little as 37.5m wide (inline), with finite beds on the order of 1.5–3.0m thick (assuming 1,600m/s). The left blow-up (Fig 4b) highlights gas migration along a fault that intersects the sea floor. The base of the visible gas anomaly spans approximately 15.6m inline distance. Fig 5 shows the level of detail recorded near the sea floor. Because of the preliminary nature of these data, the sea floor was picked at the first zero amplitude positive to negative phase transition approximately 0.005s TWT below the
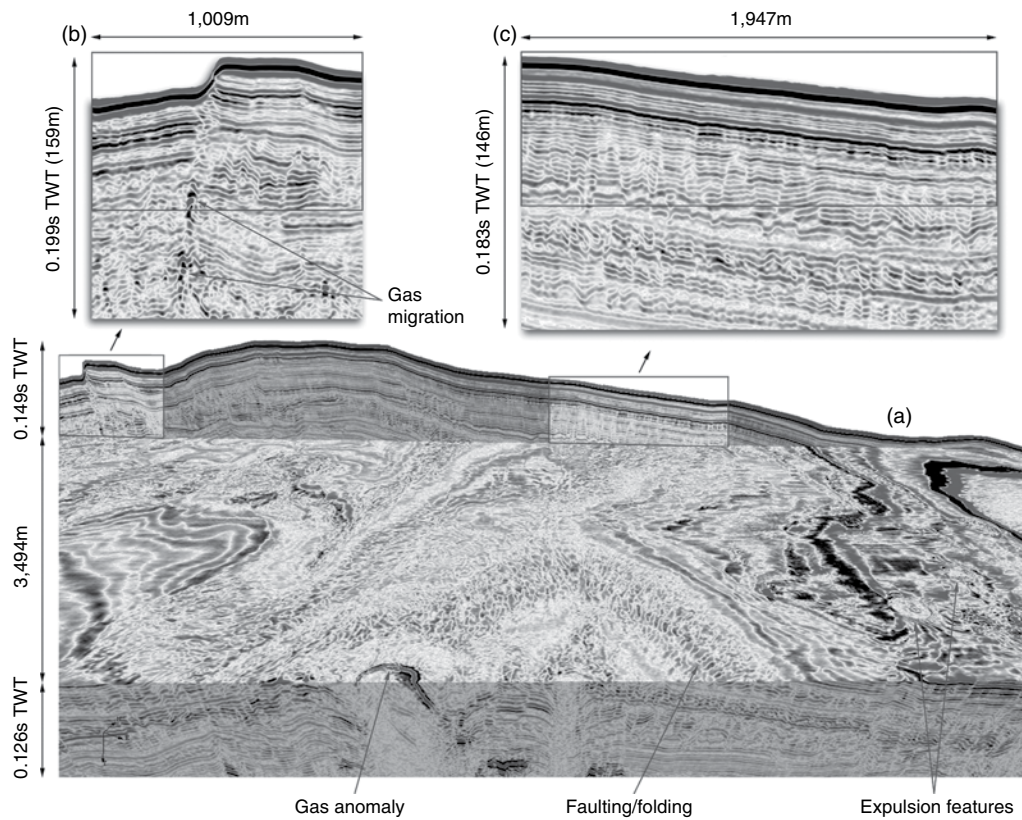
Fig 4: (a) Perspective chair-cut illustrating shallow subsurface resolution; (b) blow-up of gas migration along a fault intersecting the sea floor; and (c) blow-up of fine-scale faulting, displaced blocks and narrow beds
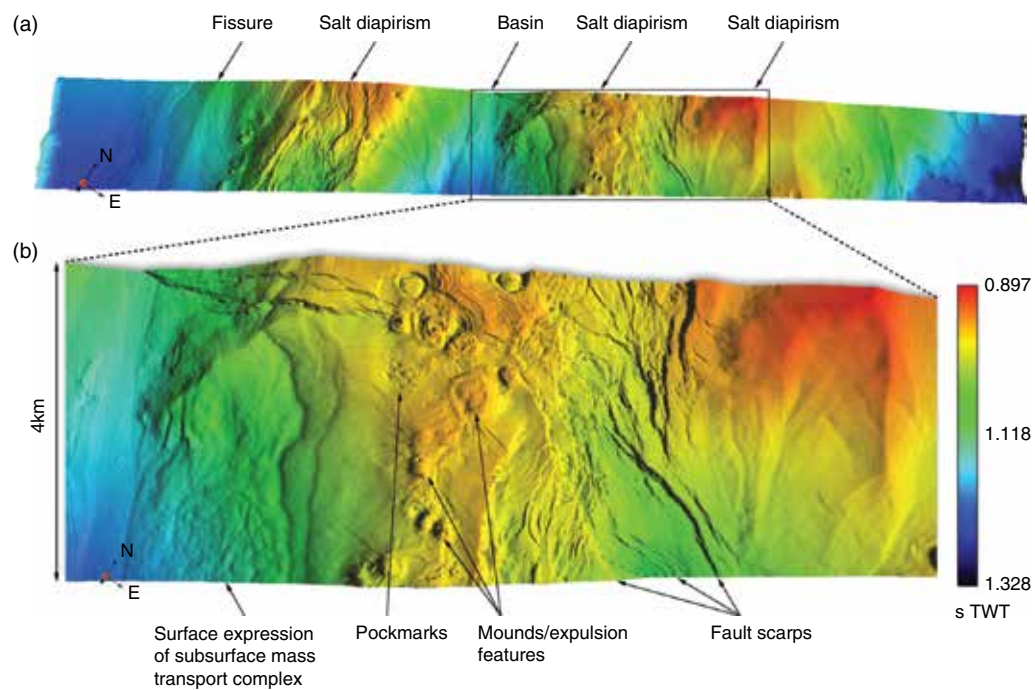

Fig 5: (a) Overview rendering of sea floor horizon illustrating bathymetric trends; and (b) blow-up of seafloor horizon illustrating mounds/expulsion features, pock marks, fault scarps and other details of the seafloor geomorphology

actual sea floor. The resulting image reveals aspects of the seafloor geomorphology on multiple scales. Clearly visible are salt-related bathymetric highs/ lows, mass transport complexes, fissures, fault scarps, mounds/expulsion features and pockmarks.

4. Discussion and conclusions

The data, in spite of their preliminary state, effectively address the questions posed in the introduction of the present paper. The penetration, on the order of 2s TWT below the seabed, is consistent with the expectations based on computer modelling of the source. Even more importantly, it aligns with numerous discussions with seasoned industry experts who have empirical observation of sufficient penetration with relatively small air volumes. The present study was successful in imaging dips in excess of 17°. For comparative purposes, the regional gradient from 100–3,000m along the northern Gulf of Mexico continental slope is about 1°. The average slope of the Sigsbee Escarpment is approximately 6°, with more localised slopes of 9°. The greatest slopes in the Gulf of Mexico, like those found along the flanks of Orca Basin, approach 20° (Bryant et al., 1990). Therefore, it is possible to image relatively steep dips at mid-slope depths (~1,000m) in the northern Gulf of Mexico with the relatively short offsets employed in P-Cable™ acquisition.

There are illumination limitations with the P-Cable™ technology, but these result primarily from impedance contrast obstacles, such as free gas for which the offsets are not great enough to under-shoot. The frequencies recovered are of sufficient bandwidth to allow extremely high-resolution imaging over at least the upper second of penetration. The imaging of very fine-scale subsurface structures, such as faults and gas anomalies, illustrates the ultra-high-resolution nature of these data. Although there are not any direct comparisons to multi-beam sonar data, the spatial resolution of the interpreted sea floor appears to rival that of bathymetric data collected by ship-mounted multi-beam sonar, which is on the order of tens of metres at depths approaching 1,000m. The present study's success in acquiring, and subsequently processing, these data at the natural bin size of 3.125 × 6.25m was facilitated by the ability to monitor the actual geometry of the receiver array and scrutinise positioning quality control measures in real time. This is an advantage over methodologies that rely on an assumed geometry during acquisition (e.g. Petersen et al., 2010).

The aims of a future, more thoroughly processed dataset include extra steps that would help pull even more information from the already useful data. These include multiple attenuation, interpolation of missing bins, pre-stack time migration, advanced post-stack processing and HDBAND™ (to attenuate source and receiver ghosts). The de-multiple scheme uses an iterative 2D SRME approach, including shot interpolation from a spacing of 12.5–6.25m to satisfy geometry requirements, as well as trace extrapolation back to zero and negative offsets. The final subtraction of the multiple model from the data is done in the common channel domain to remove as much of the 1st and 2nd order water bottom multiple as possible. The SRME method utilises the general wave equation boundary condition and makes no assumptions regarding wave behaviour in the earth. Therefore, no prior model or knowledge of the subsurface is necessary, which works quite well on such short streamer data where a lack of move-out does not allow for Radon de-multiple techniques. The removal of the unwanted, multiple energy prevents smearing and introduction of unwanted artefacts into the shallow section during the final pre-stack time migration. This allows for expanded use of the dataset for identification of even deeper geohazards and exploration targets. The HDBAND™ suite, for ghost attenuation, is flexible in allowing for application either pre- or post-stack and either pre- or post-migration. The known ghost problem leaves notches in the frequency spectrum, which leads to a loss of resolution and blurry or band limited images. Removal of the ghost frequency notches results in a sharper, cleaner product yielding an even higher resolution than on input.

UHR3D seismic data certainly present their share of challenges, both operationally and during processing, but the authors are confident that this is the way forward for the marine geohazards and near-surface marine geophysics community. The ability to accurately identify and delineate geohazards and drilling risks undoubtedly justifies the added costs of utilising this methodology to supplement traditional deep penetration seismic. As more data are presented in the public domain, the broader geoscience industry will be made aware of the acute relevance of this technology.

References

Brooks JM, Cox BH, Bryant WR and Kennicutt MC. (1986). Association of gas hydrates and oil seepage in the Gulf of Mexico. *Organic Chemistry* **10**: 221–234.

Bryant WR, Bryant JR, Freely MH and Simmons GR. (1990). Physiographic and bathymetric characteristics of the continental slope, northwest Gulf of Mexico. *Geo-Marine Letters* **10**: 182–199.

Crutchley GJ, Berndt C, Klaeschen D and Masson DG. (2011). Insights into active deformation in the Gulf of Cadiz from new 3-D seismic and high-resolution bathymetry. *Geochemistry, Geophysics, Geosystems* **12**: Q07016.

Crutchley GJ, Karstens J, Berndt C, Talling PJ, Watt SFL, Vardy ME, Huhnerbach V, Urlaub M, Sarkar S, Klaeschen D, Paulatto M, Le Friant A, Lebas E and Maeno F. (2013). Insights into the emplacement dynamics of volcanic landslides from high-resolution 3D seismic data acquired offshore Montserrat, Lesser Antilles. *Marine Geology* **335**: 1–15.

Diegel FA, Karlo JF, Schuster DC, Shoup RC and Tauvers PR. (1995). Cenozoic structural evolution and tectono-stratigraphic framework of the northern Gulf Coast continental margin. In: Jackson MPA, Roberts DG and Snelson S. (eds.). *Salt Tectonics: A Global Perspective.* Tulsa, Oklahoma: American Association of Petroleum Geologists, 109–151.

Games KP. (2012). Shallow gas detection – why HRS, why 3D, why not HRS 3D? *First Break* **30**: 67–75.

Holbrook WS. (2001). Seismic studies of the Blake Ridge: Implications for hydrate distribution, methane expulsion and free gas dynamics. In: Paull CK and Dillon WP. (eds.). *Natural Gas Hydrates: Occurrence, Distribution, and Detection.* Washington, DC: American Geophysical Union, 235–256.

MacDonald IR, Guinasso NL, Sassen R, Brooks JM, Lee L and Scott KT. (1994). Gas hydrate that breaches the sea floor on the continental slope of the Gulf of Mexico. *Geology* **22**: 699–702.

Marfurt KJ. (2006). Robust estimates of 3D reflector dip and azimuth. *Geophysics* **71**: 29–40.

Petersen CJ, Bunz S, Hustoft S, Mienert J and Klaeschen D. (2010). High-resolution P-Cable 3D seismic imaging of gas chimney structures in gas hydrated sediments of an Arctic sediment drift. *Marine and Petroleum Geology* **27**: 1,981–1,994.

Plaza-Faverola A, Bunz S and Mienert J. (2011). Repeated fluid expulsion through sub-seabed chimneys offshore Norway in response to glacial cycles. *Earth and Planetary Science Letters* **305**: 297–308.

Prather BE, Booth JR, Steffens GS and Craig PA. (1998). Classification, lithologic calibration, and stratigraphic succession of seismic facies of intraslope basins, deep-water Gulf of Mexico. *AAPG Bulletin* **82**: 701–728.

Roberts HH. (2001). Fluid and gas expulsion on the northern Gulf of Mexico continental slope: mud-prone to mineral-prone responses. In: Paull CK and Dillon WP. (eds.). *Natural Gas Hydrates: Occurrence, Distribution, and Detection.* Washington: American Geophysical Union, 145–161.

Sager WW, MacDonald IR and Hou R. (2003). Geophysical signatures of mud mounds at hydrocarbon seeps on the Louisiana continental slope, northern Gulf of Mexico. *Marine Geology* **198**: 97–132.

Sheriff RE. (2002). *Encyclopedic Dictionary of Applied Geophysics.* Fourth edition. Tulsa: Society of Exploration Geophysicists, 429pp.

Sturges W and Leben R. (2000). Frequency of ring separations from the Loop Current in the Gulf of Mexico: a revised estimate. *Journal of Physical Oceanography* **30**: 1,814–1,819.

Vermeer GJ. (2012). *3D Seismic Survey Design.* Second edition. Tulsa: Society of Exploration Geophysicists, 164pp.